A Modeling Study of Summertime East Pacific Wind-Induced Ocean–Atmosphere Exchange in the Intraseasonal Oscillation

ERIC D. MALONEY AND STEVEN K. ESBENSEN

College of Oceanic and Atmospheric Sciences, Oregon State University, Corvallis, Oregon

(Manuscript received 14 April 2004, in final form 6 August 2004)

ABSTRACT

Intraseasonal precipitation variability over the northeast Pacific warm pool during June–October in the National Center for Atmospheric Research Community Atmosphere Model 2.0.1 with a relaxed Arakawa–Schubert convection parameterization is found to be strongly sensitive to wind-induced variations in surface latent heat flux. A control simulation with interactive surface fluxes produces northeast Pacific warm pool intraseasonal wind and precipitation variations that are of similar magnitude and structure to those associated with the observed intraseasonal oscillation (ISO). Periods of low-level westerly intraseasonal wind anomalies are associated with enhanced surface latent heat fluxes and enhanced precipitation, as in observations. Variations in surface wind speed primarily control the surface flux anomalies.

A simulation in which eastern North Pacific oceanic latent heat fluxes are fixed produces intraseasonal precipitation variations that are significantly weaker than those in the control simulation and in observations. These results support the observational findings of Maloney and Esbensen, who suggested that wind-induced latent heat flux variability is a significant driver of ISO-related convective variability over the northeast Pacific warm pool during Northern Hemisphere summer. East Pacific ISO-related convection in this model, thus, appears to be forced by an analogous wind-induced surface heat exchange mechanism to that proposed by Maloney and Sobel to explain the forcing of west Pacific ISO-related convection. The surface exchange mechanism is apparently active within regions of mean westerly low-level flow.

In contrast, summertime eastern North Pacific intraseasonal wind variance and spatial structure does not differ significantly between the control and fixed-evaporation simulations. A strong coupling between the east Pacific flow and precipitation over Central America may be responsible for the relatively small changes in wind variability between the simulations. Interactions among the coarsely resolved Central American orography, the large-scale flow, and the convection parameterization in the model likely contribute to this anomalous coupling.

1. Introduction

Maloney and Esbensen (2003, hereafter ME03) showed that a strong relationship exists between observed summertime eastern North Pacific convection and latent heat flux anomalies during intraseasonal oscillation (ISO) events (e.g., Madden and Julian 1994). Enhanced latent heat flux and enhanced convection are associated with westerly anomalies in the low-level flow over the northeast Pacific warm pool. The latent heat flux anomalies are primarily controlled by anomalies in surface wind speed. This relationship suggests that a wind-induced surface exchange mechanism may be important in forcing east Pacific intraseasonal convection anomalies. The enhancement of latent heat flux anomalies within anomalous westerly flow (rather than easterly flow) suggests that a somewhat different wind–evaporation feedback mechanism than that originally proposed by Neelin et al. (1987) and Emanuel (1987) may be important for forcing ISO convection over the east Pacific warm pool where low-level summer mean winds are from the west. A recent modeling study suggests that a similar nonlinear wind–evaporation feedback mechanism may help support intraseasonal convection over the west Pacific warm pool during wintertime (Maloney and Sobel 2004). It is also notable that periods of westerly winds and enhanced latent heat fluxes were accompanied by enhanced warm pool precipitation during the East Pacific Investigation of Climate (EPIC) 2001 experiment (Raymond et al. 2003). Some of the flux variability observed during EPIC 2001 was likely related to the passage of an intraseasonal oscillation event (E. Maloney 2003, unpublished data). A more general overview of summertime intraseasonal variability in the Americas can be found in the recent literature (e.g., Knutson and Weickmann 1987; Kayano and Kousky 1999; Magaña et al. 1999; Maloney and

Corresponding author address: Eric D. Maloney, College of Oceanic and Atmospheric Sciences, Oregon State University, 104 Ocean Admin Building, Corvallis, OR 97331-5503.
E-mail: maloney@coas.oregonstate.edu

Hartmann 2000; Higgins and Shi 2001; Maloney and Kiehl 2002a).

ME03 suggested that the sensitivity of east Pacific ISO convection to wind-induced latent heat flux variability could be tested using an appropriate modeling study in which east Pacific surface evaporation is set to its climatological seasonal cycle. We will conduct such a study here. Maloney and Sobel (2004) showed that the modified National Center for Atmospheric Research (NCAR) Community Atmosphere Model 2.0.1 (CAM2.0.1) with a relaxed Arakawa–Schubert convection parameterization (RAS; Moorthi and Suarez 1992) produces equatorial Pacific intraseasonal anomalies in winds and convection that have eastward propagation speeds ($\sim$5–6 m s^{-1}) and amplitudes comparable to observations. Maloney and Sobel (2004) analyzed boreal winter behavior in the eastern hemisphere, whereas this study will examine boreal summer behavior over the eastern North Pacific warm pool. Surface evaporation variations forced by anomalies in surface wind speed were crucial for producing realistic intraseasonal convective variability across the west Pacific in the model of Maloney and Sobel (2004). In simulations that included an interactive slab ocean, reducing the oceanic mixed layer depth to 2 m limits the exchange of latent energy between the ocean and atmosphere on intraseasonal time scales, thereby strongly reducing intraseasonal convection variations. This 2-m mixed layer simulation was analogous to one in which surface latent heat fluxes were prescribed by their climatological seasonal cycle. Exchange of energy between the ocean and atmosphere and intraseasonal convective variability was greatest for a mixed layer depth of 20 m.

We will here examine June–October east Pacific intraseasonal variability in a control simulation forced by climatological SSTs, and will compare the behavior in this simulation to a simulation experiment in which east Pacific warm pool latent heat fluxes are also set to their climatological values. Variations in wind speed strongly dominate model intraseasonal latent heat flux variability in the east Pacific warm pool. The fixed-evaporation experiment essentially eliminates wind–evaporation feedback. Surface heat fluxes outside of the east Pacific remain fully interactive to limit the possibility that changes occurring elsewhere in the Tropics influence the simulation of intraseasonal variability over the east Pacific warm pool.

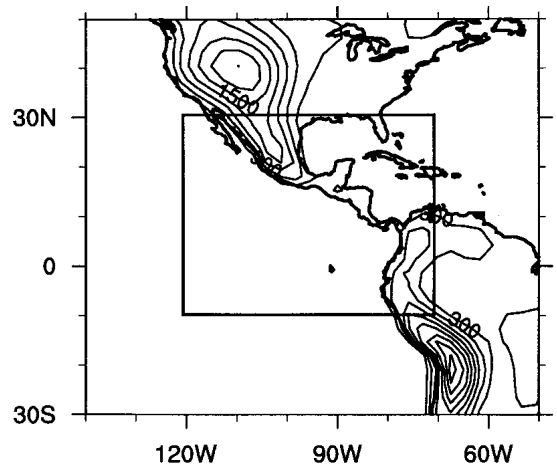

FIG. 1. The representation of east Pacific orography in the model and the domain over which surface latent heat fluxes are set to their climatological seasonal cycle in the fixed-EVAP simulation. The contour interval is 300 m.

Section 2 describes the model simulations and the observational datasets used in this study. Section 3 compares the June–October east Pacific mean state and compares broader measures of intraseasonal precipitation and wind variability among the observations and two simulations. Section 4 examines composite east Pacific ISO behavior in the models using the global ISO 850-hPa zonal wind field as a basis for compositing. Section 5 presents conclusions.

2. Model and data description

a. NCAR CAM2.0.1 with RAS convection

A modified version of the NCAR CAM2.0.1 (information is available online at http://www.ccsm.ucar.edu/) is used in this study. Because the standard CAM2.0.1 deep convection parameterization of Zhang and McFarlane (1995) produces intraseasonal variability that is significantly weaker than observed (e.g., Maloney and Hartmann 2001), we have implemented the RAS convection scheme of Moorthi and Suarez (1992) to simulate deep convection. The RAS parameterization produces realistic tropical intraseasonal variability in various versions of the NCAR CAM (e.g., Maloney and Kiehl 2002b; Maloney and Sobel 2004). We use a version of RAS that allows convective rainfall to cool and moisten the environment by evaporation, as described in Sud and Molod (1988). Dynamic downdrafts are not explicitly driven by this evaporative cooling, however. Hence, the ability of convection to decrease boundary layer moist static energy may be underrepresented in the model (e.g., Betts 1976). The Hack (1994) convection parameterization remains as the shallow convection scheme in our modified version of CAM2.0.1.

The CAM2.0.1 is a global model integrated at T42 horizontal resolution in the simulations described below. This truncation corresponds to a grid resolution of approximately 2.8° latitude $\times$ 2.8° longitude. CAM2.0.1 grid cells include fractional land/ocean areas, meaning that a given 2.8° $\times$ 2.8° cell along a coastline could be a blend of land and ocean. Twenty-six levels in the vertical are resolved, and the model time step is 20 min.

Figure 1 gives the representation of model orography over the tropical Western Hemisphere. The orography of the Americas is admittedly rather coarsely resolved.

Despite this coarse resolution, the model still does a reasonable job in simulating realistic intraseasonal variability in this region, as will be described in subsequent sections. Nevertheless, some aspects of the simulation appear to be somewhat unrealistic due to the coarse resolution of orography, and these will be discussed below.

b. Experiments

Two 15-yr simulations forced by climatological sea surface temperatures are initially conducted. Oceanic surface latent heat fluxes in the second simulation are set to the climatological seasonal cycle from the first simulation in the domain indicated by the inner box of Fig. 1. A 10° buffer is imposed around this box in which the imposition of climatological surface fluxes decays exponentially to zero at the outer boundary of Fig. 1 and blends with interactive surface fluxes. Fluxes over land are allowed to remain fully interactive in both simulations, given the expectation from ME03 that oceanic, rather than land, latent heat flux variations are the primary driver of intraseasonal convection variations near the Americas. The two simulations will hereafter be referred to as the "control" and "fixed evaporation (fixed EVAP)" simulations.

Because precipitation over Central America appears to play a significant role in the model ISO, an additional 15-yr simulation is conducted in which the surface type is set to the ocean everywhere within the domain 10°–30°N, 80°–120°W, and surface temperatures and latent heat fluxes were set to the climatology from the control simulation. We also allow surface geopotential height to remain unchanged from the control. This experiment should help to distinguish whether surface type or representation of orography is most important for generating intraseasonal precipitation variations over Central America, and should help determine whether factors such as the finite heat capacity of the land surface or variations in soil moisture contribute importantly to model intraseasonal precipitation variations there. This simulation will be referred to as the "no land" simulation.

c. Observed data products

A limited comparison of model results to observations is made here, although more detailed observational analyses of east Pacific ISO variability can be found in previous studies (e.g., ME03; Maloney and Kiehl 2002a,b). Surface and 850-hPa vector winds and surface latent heat fluxes during 1979–99 are obtained from the National Centers for Environmental Prediction (NCEP)–NCAR gridded (2.5° × 2.5°) reanalysis dataset (Kalnay et al. 1996). The Climate Prediction Center (CPC) Merged Analysis of Precipitation (CMAP) gridded (2.5° × 2.5°) precipitation fields are used during 1979–99 (Xie and Arkin 1996). These data were interpolated from pentad means to daily values in the composite analysis of intraseasonal variability shown below. Summertime mean fields from the merged Tropical Rainfall Measuring Mission (TRMM) precipitation product (1° × 1°) during 1998–2002 are also used in the mean state comparison (e.g., Kummerow et al. 2000).

3. Results: Model climate and intraseasonal variance

a. Comparison of June–October means

Figure 2 shows average June–October surface wind vectors from NCEP–NCAR reanalysis, the control simulation, and the fixed-EVAP simulation. The mean low-level flow is quite similar among the reanalysis product and models, although subtle differences exist on closer inspection. One difference is that easterly

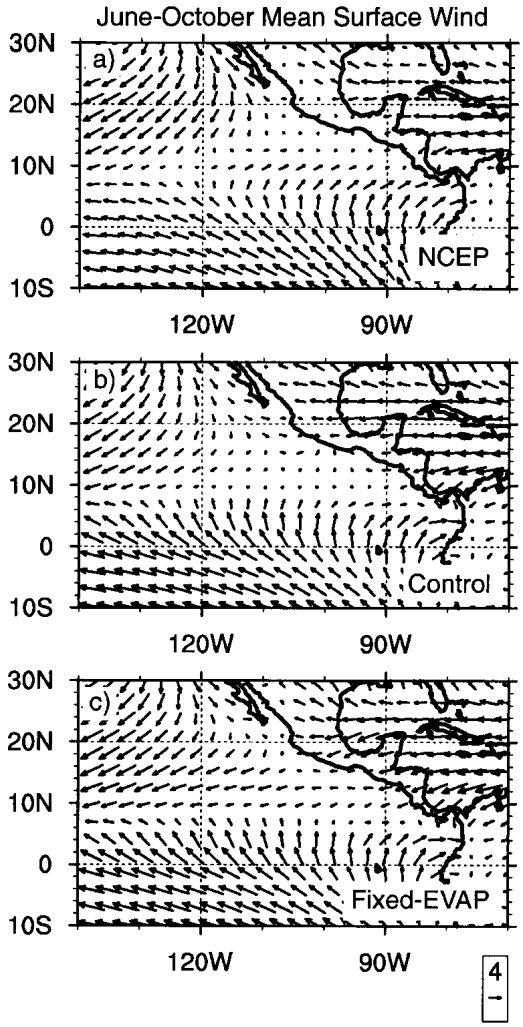

FIG. 2. Mean Jun–Oct surface winds from (a) NCEP–NCAR reanalysis, (b) the control simulation, and (c) the fixed-EVAP simulation.

flow in the two simulations tends to be stronger over Mexico and Central America than in the reanalysis. This stronger low-level flow over land is likely a by-product of the coarse resolution of model land surface orography and the reduced blocking of the low-level flow. Some of this easterly bias may also be due to quasigeostrophic adjustment to anomalous diabatic heating over land, the presence of which will become evident when examining the climatological precipitation distributions below. Another difference among the panels is that weak easterly flow tends to occur over the east Pacific warm pool in the fixed-EVAP simulation as compared to weak westerly flow in the reanalysis and control simulation. Cross-equatorial flow tends to be somewhat stronger in the simulations than in the reanalysis, although previous work using scatterometer vector winds has suggested that the NCEP–NCAR reanalysis product may underestimate cross-equatorial flow (Milliff et al. 1999).

A comparison of average June–October precipitation fields among CMAP, TRMM, and the simulations is shown in Fig. 3. CMAP and TRMM provide independent precipitation estimates. Although the observed fields are generally similar between the CMAP and TRMM products, one major difference between them is that the TRMM product ($1° \times 1°$) resolves the well-documented precipitation maximum in the Bight of Panama (e.g., Mapes et al. 2003), whereas the coarser-resolution CMAP climatology does not. Although records of different length were used to calculate climatologies in CMAP and TRMM, resolution of the Bight of Panama feature is insensitive to the length of record over which the averages were computed. Both simulations overpredict precipitation in the bight region and in southern Mexico, and underpredict precipitation in the intertropical convergence zone. Some of these deficiencies, particularly the anomalously high precipitation over Mexico, are likely due to the coarse resolution of topography in CAM2.0.1. Some reduction in mean precipitation over Mexico occurs in the fixed-EVAP simulation, which is likely related to the appearance of weak easterlies over the east Pacific warm pool in that simulation and reduced onshore moisture advection.

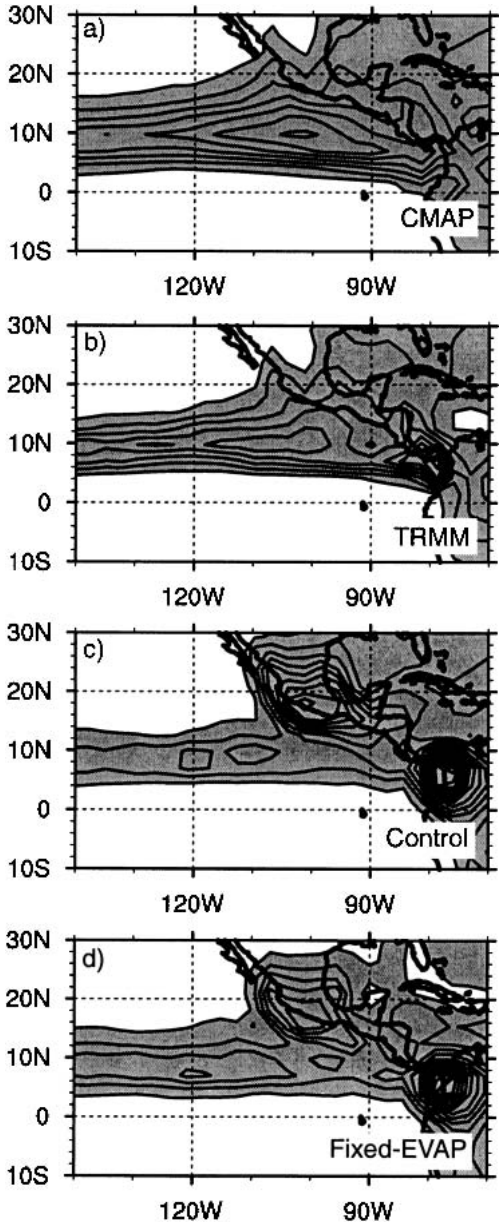

FIG. 3. Mean Jun–October observed precipitation from (a) CMAP and (b) TRMM, and modeled precipitation from the (c) control and (d) fixed-EVAP simulations. The contour interval is 2 mm day^{-1}. Values greater than 2 mm day^{-1} are shaded.

b. Intraseasonal variance

Intraseasonal variability is examined by filtering fields using a linear nonrecursive filter with half-power points at 30 and 90 days. Figure 4 shows June–October intraseasonal precipitation variance over the east Pacific Ocean from CMAP and from the simulations. Values over land are masked in this plot to highlight oceanic anomalies. Behavior of anomalies over land will be discussed in more detail below. Removing points that contain some percentage of land indicates that the intraseasonal variance patterns in Fig. 4 and the differences among them are quite similar if only pure ocean points are considered.

Intraseasonal precipitation variance over the eastern North Pacific warm pool is significantly higher during June–October in the control simulation than in the fixed-EVAP simulation. Variance in the control simulation peaks near 18 mm^2 day^{-2}, as opposed to 8 mm^2 day^{-2} in the fixed-EVAP simulation. The variance maximum in the control simulation is of more realistic magnitude and spatial extent than that of the fixed-EVAP simulation. CMAP precipitation variance peaks near 14 mm^2 day^{-2}. The variance maximum in the con-

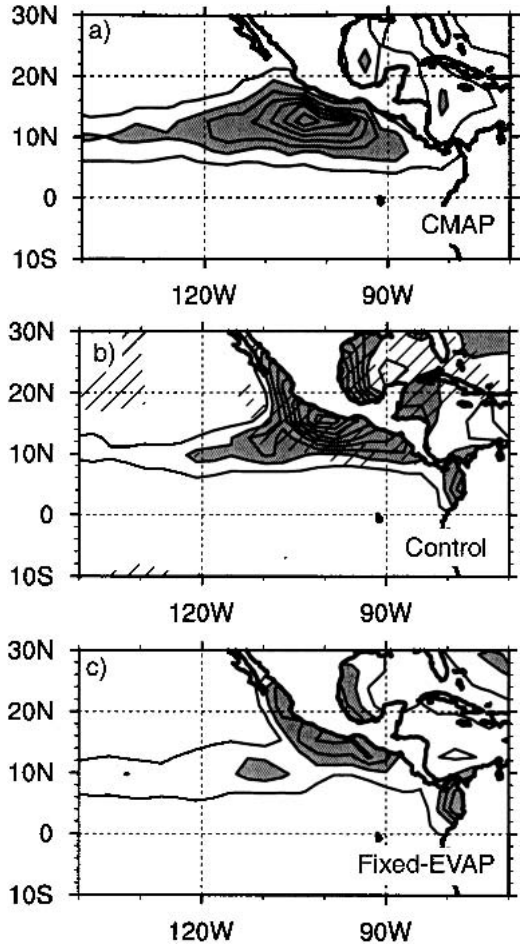

FIG. 4. Jun–Oct 30–90-day precipitation variance from (a) CMAP, (b) the control simulation, and (c) the fixed-EVAP simulation. The contour interval is 2 mm^2 day^{-2}. Values greater than 4 mm^2 day^{-2} are shaded. Diagonal lines in (b) indicate where the fixed-EVAP variance falls below the lower 95% confidence limit on the control variance.

trol simulation is shifted slightly to the northeast of that in CMAP, which is likely due to the coarse resolution of the model orography. Recall the tendency for the CAM2.0.1 with RAS convection to overpredict precipitation near and over the Central American landmass (Fig. 3). Diagonal lines in Fig. 4b indicate where precipitation variance in the fixed-EVAP simulation falls below the lower 95% confidence interval on the control simulation variance using the χ^2 statistic. We have assumed that each 50-day period represents an independent sample, a justifiable assumption given that little correlation exists between adjacent ISO events in observations (e.g., Hendon and Salby 1994). This gives approximately 40 degrees of freedom for the simulated record, a more conservative estimate of the degrees of freedom than would be obtained by using the *e*-folding or first zero-crossing autocorrelation times.

Power spectra of precipitation for an approximate 5° × 5° averaging box centered at 14°N, 102°W are shown in Fig. 5 for the control simulation and the fixed-EVAP simulation. Shown also are the red noise spectral and the a priori 95% confidence limits on the red noise spectra. This averaging box corresponds to the location of maximum precipitation variance in the control and fixed-EVAP simulations (Fig. 4). These spectra can be compared to the observed precipitation spectrum in Fig. 1 of ME03. The control spectrum has a significant spectral peak centered near a period of 50 days, consistent with the observed 50-day peak found in observations (ME03). The control simulation peak is somewhat

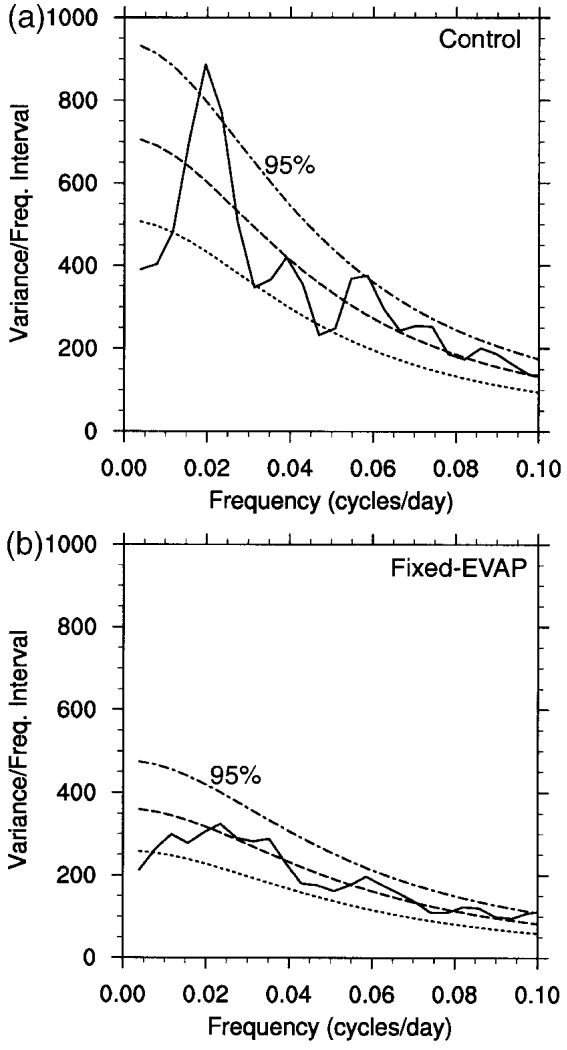

FIG. 5. Power spectrum of precipitation for an approximate 5° × 5° averaging box centered at 14°N, 102°W for the (a) control and (b) fixed-EVAP simulations. Spectra are the average of 14 spectral estimates of individual 256-day time series centered on Aug of each year. A cosine taper was applied to the ends of each time series before spectra were computed. The red noise spectra and associated 95% upper and lower confidence limits are also displayed. The seasonal cycle was removed before computation of the spectra. The spectra are normalized such that the area under the curve equals the total variance.

less prominent than that in observations. The spectrum for the fixed-EVAP simulation looks primarily red with no significant spectral peak at intraseasonal time scales, suggesting that interactive latent heat fluxes are necessary for producing realistic summertime intraseasonal precipitation variations over the eastern North Pacific warm pool. These results thus support the observational findings of ME03, and will be further explored below.

Interestingly, east Pacific June–October surface zonal wind variance does not differ significantly between the control and fixed-EVAP simulations (Fig. 6). The spatial structure and magnitude of zonal wind variance in the control and fixed-EVAP simulations are similar to that observed. The control simulation tends to have somewhat higher variance near the south Mexican coast than in the fixed-EVAP simulation. Maloney and Kiehl (2002b) found that east Pacific intraseasonal zonal wind variability in a previous version of the NCAR CAM with RAS convection was strongly tied to precipitation variability over the Central American landmass. They attributed this anomalous coupling to the coarse resolution of orography in the model. A similar strong coupling between latent heating over land and oceanic wind variability may exist in the NCAR CAM2.0.1 with RAS convection. Results presented below will help elucidate this relationship, and show that mostly energy conversions over land support modeled large-scale circulation anomalies near the Americas.

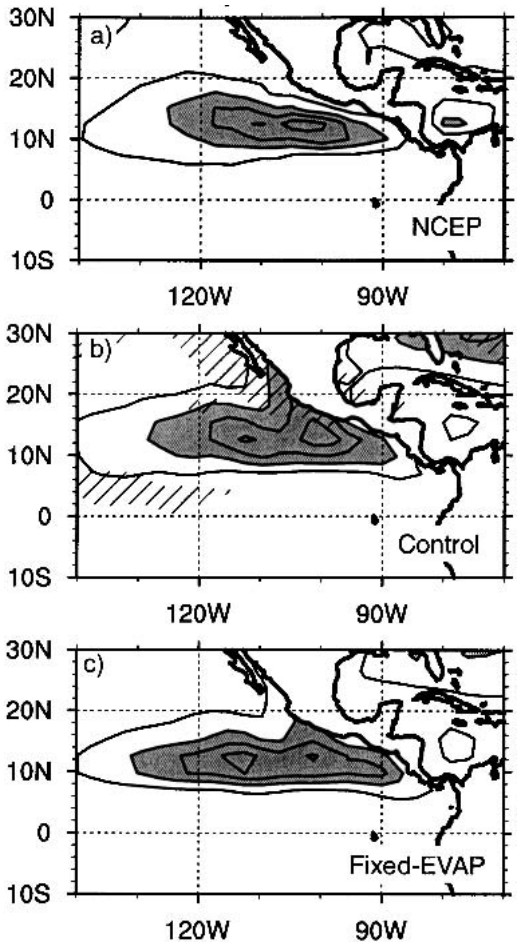

FIG. 6. Jun–Oct 30–90-day surface zonal wind variance from (a) NCEP–NCAR reanalysis, (b) the control simulation, and (c) the fixed-EVAP simulation. The contour interval is 0.8 $m^2 s^{-2}$. Values greater than 1.6 $m^2 s^{-2}$ are shaded. Diagonal lines in (b) indicate where the fixed-EVAP variance falls below the lower 95% percent confidence limit on the control variance.

4. Results: A composite model intraseasonal oscillation

a. Compositing technique

Composite ISO events over the east Pacific during June–October will now be examined in both simulations. Composites will be created by averaging with respect to an index that describes global equatorial ISO zonal wind variability. Using such a global index will ensure as uniform a compositing technique as possible between the control and fixed-EVAP simulation because fully interactive surface fluxes are allowed outside of the east Pacific warm pool region in the fixed-EVAP simulation, and changes to ISO behavior outside of the east Pacific are minimized.

A brief justification for using zonal wind as a compositing index will now be provided. Figure 7 shows average wavenumber–frequency spectra of equatorial averaged 850-hPa zonal wind for observations and both simulations. The only prefiltering done on these fields was to remove periods greater than 150 days. We have verified that this prefiltering does not artificially create the variance maxima that are shown in the plots. Time series of equatorial-averaged (8°N–8°S) zonal winds for each longitude are used in the calculation of the spectra. Spectra reflect the average of multiple overlapping 64-pentad records that include all seasons of data. As in observations, both control and fixed-EVAP simulations are characterized by enhanced eastward spectral power at wavenumber 1 and periods of 30–80 days. Magnitudes are comparable among the models and observations, although variance in the fixed-EVAP simulation at 30–80 day periods is slightly lower than the control. These differences are not statistically significant, however. Maloney and Sobel (2004) showed that the propagation speed of control simulation intraseasonal zonal wind anomalies across the western and central Pacific is eastward at about 5 m s^{-1}, comparable to the propagation speed of the observed ISO.

Eastward propagating ISO-related equatorial zonal wind anomalies can be represented by a quadrature pair of empirical orthogonal functions (EOFs) (Kutzbach 1967). Such a quadrature pair has been used extensively in previous studies to diagnose eastward-

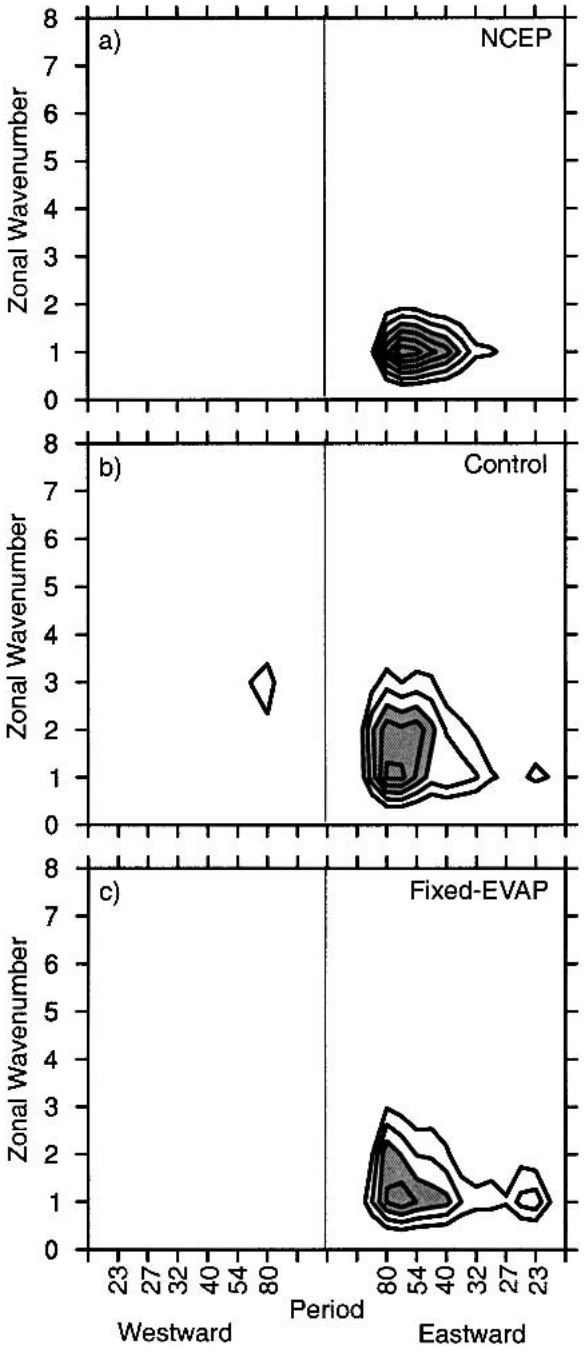

FIG. 7. Wavenumber–frequency spectrum of equatorial 850-hPa zonal wind from (a) NCEP–NCAR reanalysis, (b) the control simulation, and (c) the fixed-EVAP simulation. Contour interval is 0.006 $m^2 s^{-2}$, starting at 0.016 $m^2 s^{-2}$. Values greater than 0.028 $m^2 s^{-2}$ are shaded.

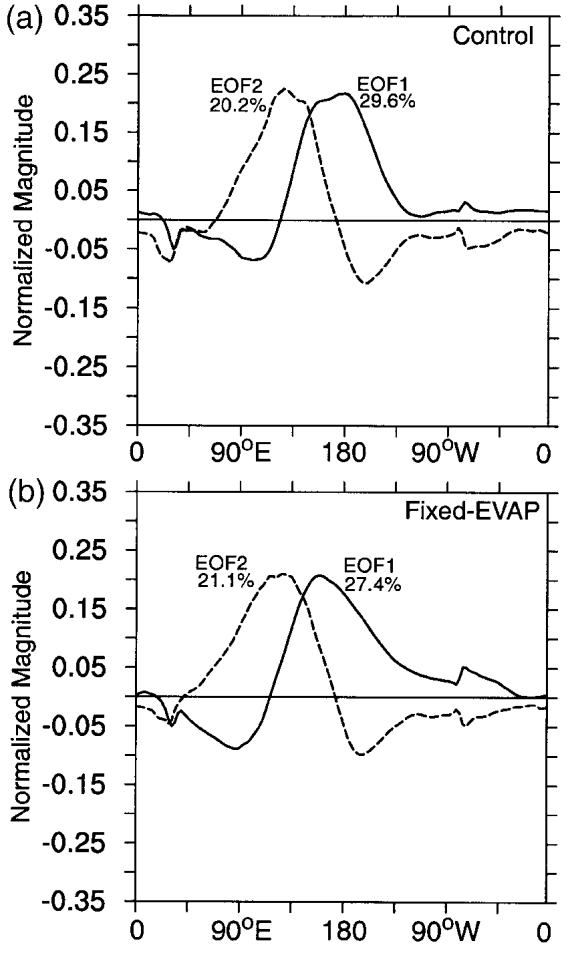

FIG. 8. Leading EOFs of the equatorial averaged (8°N–8°S) 30–90-day 850-hPa zonal wind from the (a) control simulation and (b) fixed-EVAP simulation. Magnitudes are normalized. The percent variance explained by each EOF is indicated.

propagating ISO variability in observations and models (e.g., Maloney and Hartmann 1998; Maloney and Kiehl 2002a,b; Bond and Vecchi 2003). Figure 8 shows the leading EOFs of the 30–90-day 850-hPa equatorial zonal wind from the control and fixed-EVAP simulations. The leading quadrature pair has similar structure and explains a similar amount of the variance (~50%) in both simulations. In both simulations, the principal component (PC) of EOF1 is correlated with the PC of EOF2 at 0.5 at a lag of 11 days, describing eastward propagation of equatorial zonal wind anomalies. A comparison with observed EOFs (e.g., Fig. 2 of Maloney and Hartmann 2000) indicates that the model EOFs have lower relative amplitude in the Indian Ocean as compared to observations—a reflection of the weaker than observed model intraseasonal variability over this basin (also shown in Maloney and Sobel 2004).

We develop a compositing index that follows as closely as possible the technique used in ME03 for the observed ISO. An index that selects strong eastward-propagating model ISO events can be constructed through a linear combination of the leading EOFs of the equatorial zonal wind. We choose to construct this index for both simulations by adding PC2 at time t to

PC1 at time $t + 11$. This index construction has been used extensively to diagnose ISO variability in previous studies (e.g., Maloney and Hartmann 1998).

Correlations of this ISO index with June–October east Pacific low-level flow anomalies maximize around 0.4–0.5 near 10°N. Although these correlations are significantly different from zero at the 95% confidence level (~0.3 threshold using t statistic and 42 dof), the ISO index developed here explains a lower fraction of the east Pacific wind variance than is observed. For example, the observed MJO index of Maloney and Hartmann (2000) was correlated at 0.74 with the low-level east Pacific flow, and the EOFs used there were characterized by a larger extension of variance into the east Pacific than the model EOFs derived here (Fig. 8). For consistency with the analysis methods previously used in observations, we use the global equatorial EOFs of Fig. 8 to construct our compositing index, although the lower east Pacific variance explained by these EOFs relative to observations should be noted. In the model, the northeast shift of the precipitation variance maximum relative to observations and the apparent strong forcing of convection anomalies over land may diminish the projection of northeast Pacific heating anomalies onto the equatorial waveguide.

June–October events are selected as periods between successive index maxima when the index attains an intervening minimum less than 0.75 σ from zero, where σ is the standard deviation of the index calculated over the entire 15-yr simulation. Events are then divided into nine phases, with phase five corresponding to the selected time of local minimum. Phase five generally corresponds to westerly 850-hPa wind anomalies to the west of the date line and easterly anomalies over the far west Pacific. Phases one and nine represent the local maxima before and after phase five, respectively. Phases three and seven correspond to the zero-crossing points before and after phase five, respectively. Phases two, four, six, and eight fill in half-way between the other phases. Using the above criteria, 20 June–October events are diagnosed in the control simulation and 24 events are diagnosed in the fixed-EVAP simulation. Composites for all nine phases are created by averaging each selected phase over all events.

b. ISO composites in control integration

An east Pacific composite ISO event for the control simulation is shown in Fig. 9. Control simulation ISO convection peaks near the Central American coast during phase four in association with strong southwesterly surface wind anomalies, consistent with observed composites (ME03). Precipitation anomalies peak near 3.0 mm day^{-1}, a similar magnitude to that associated with observed east Pacific ISO events (e.g., Fig. 7 of Maloney and Kiehl 2002b). Surface wind anomalies are also approximately of the same magnitude in the control simulation as in observations (e.g., Fig. 3 of ME03). Consistent with the intraseasonal variance plots shown earlier (Fig. 4), precipitation anomalies tend to be shifted toward the Mexican coast relative to observations. Stronger anomalies in precipitation and winds also occur over land in the control simulation than are observed. Their existence in the model is likely due to the coarse resolution of Central American orography, which provides little impediment to the development of strong, coherent precipitation and circulation anomalies over land. Similar behavior was noted in the modeling study of Maloney and Kiehl (2002b). A comparison of phases one and nine in the control simulation (not shown) indicates that a degree of asymmetry exists in the composite east Pacific ISO event. Anomalies during phase nine are stronger than those during phase one.

The leading EOF of June–October intraseasonal low-level zonal wind over the east Pacific domain (10°S–30°N, 70°–140°W, not shown) very much resembles the structure of zonal wind variations in the ISO composite life cycle of Fig. 9. The correlation of the principal component of this local east Pacific EOF with the global ISO index used in constructing model composites is marginally significant at the 95% confidence level (~0.3), indicating that processes other than eastward-propagating ISO events are also important for producing model intraseasonal variability over the east Pacific warm pool in the model. Further investigations of such mechanisms, which may include local regulation of east Pacific intraseasonal variability (e.g., Magaña et al. 1999), are beyond the scope of this paper.

Latent heat flux anomalies for the composite control simulation ISO life cycle are shown in Fig. 10. Periods of southwesterly anomalies and enhanced precipitation are associated with enhanced latent heat fluxes over and near the east Pacific warm pool. These relationships are similar to those associated with the observed ISO (Fig. 14 of ME03; Fig. 6 of Maloney and Kiehl 2002a). Model latent heat flux anomalies tend to maximize nearer the coast than those in observations, however. Flux anomalies in the model peak near 14 W m^{-2} during phase four, with the strongest negative anomalies of -22 W m^{-2} during phase nine. These magnitudes are similar to those observed.

The correlation between east Pacific precipitation and latent heat fluxes during ISO events is similar in observations and the control simulation. Figure 11 shows scatterplots of precipitation versus latent heat flux anomalies during ISO events in observations and the control simulation for $5° \times 5°$ averaging boxes centered at the respective east Pacific warm pool intraseasonal precipitation variance maximum. The linear least squares fits are displayed. Observed ISO events are defined as described in ME03. Each point in Fig. 11 represents one phase of one ISO event. Observed precipitation is averaged within a box centered at 11°N, 99°W. Because observed intraseasonal precipitation over the east Pacific warm pool is most highly correlated with surface fluxes slightly upstream (Fig. 15 of

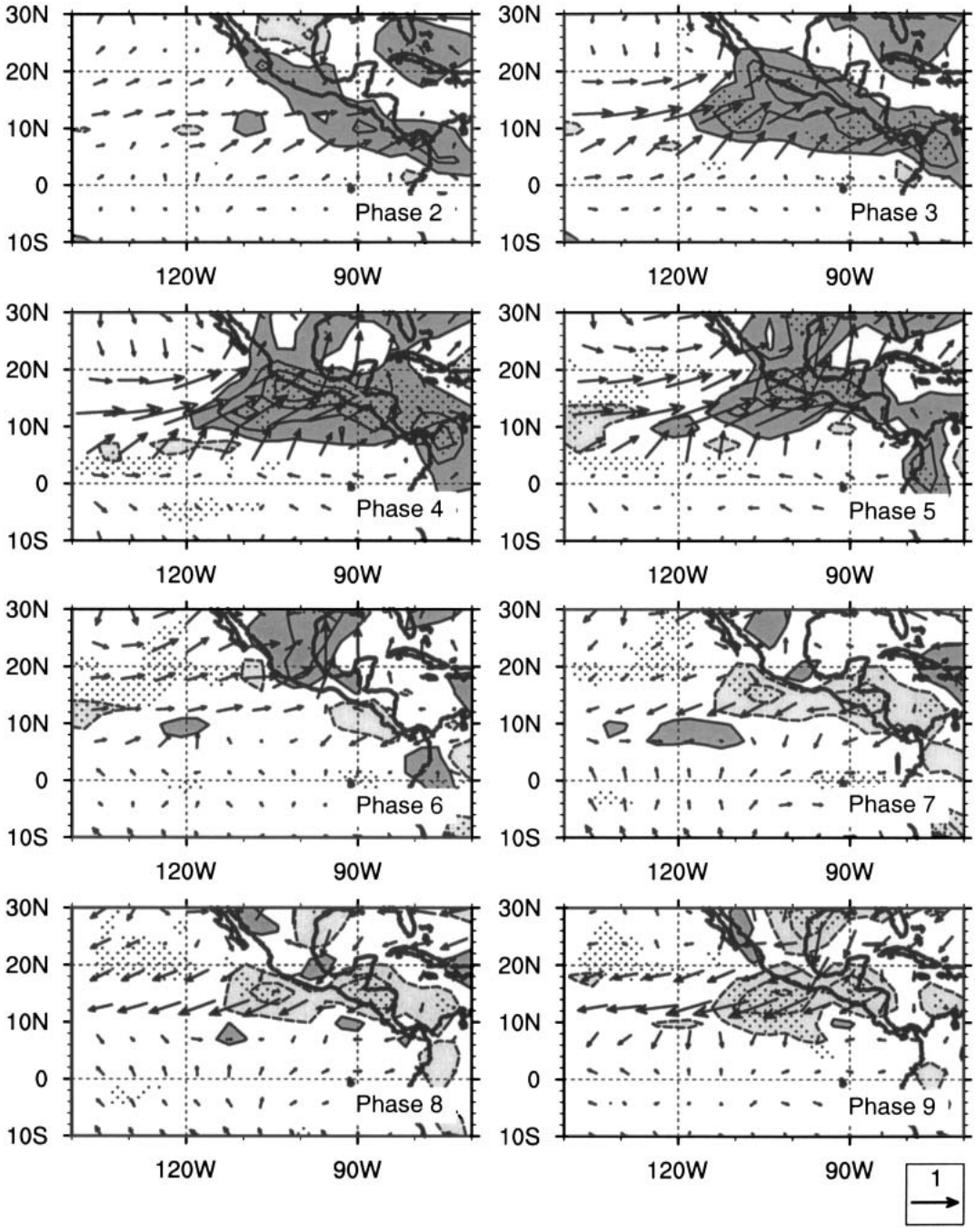

FIG. 9. Control simulation composite Jun–Oct ISO surface wind and precipitation anomalies as a function of phase. Precipitation contours are plotted every 0.8 mm day^{-1}, starting at 0.4 mm day^{-1}. Values greater (less) than 0.4 mm day^{-1} (-0.4 mm day^{-1}) are dark (light) shaded. Stippling indicates where precipitation anomalies are significantly different from zero at the 95% confidence level using the t statistic. The reference wind vector (m s^{-1}) is located at the bottom right.

ME03), the corresponding observed latent heat fluxes in Fig. 11 are calculated over a box centered at 11°N, 104°W. Control simulation–averaged precipitation and fluxes are both calculated for a box centered at 14°N, 102°W because the highest control simulation correlations occur for collocated latent heat fluxes and precipitation. Also 14°, 102°W is the location of strongest latent heat flux and precipitation anomalies. In contrast, model equatorial *west* Pacific precipitation anomalies are most highly correlated with upstream la-

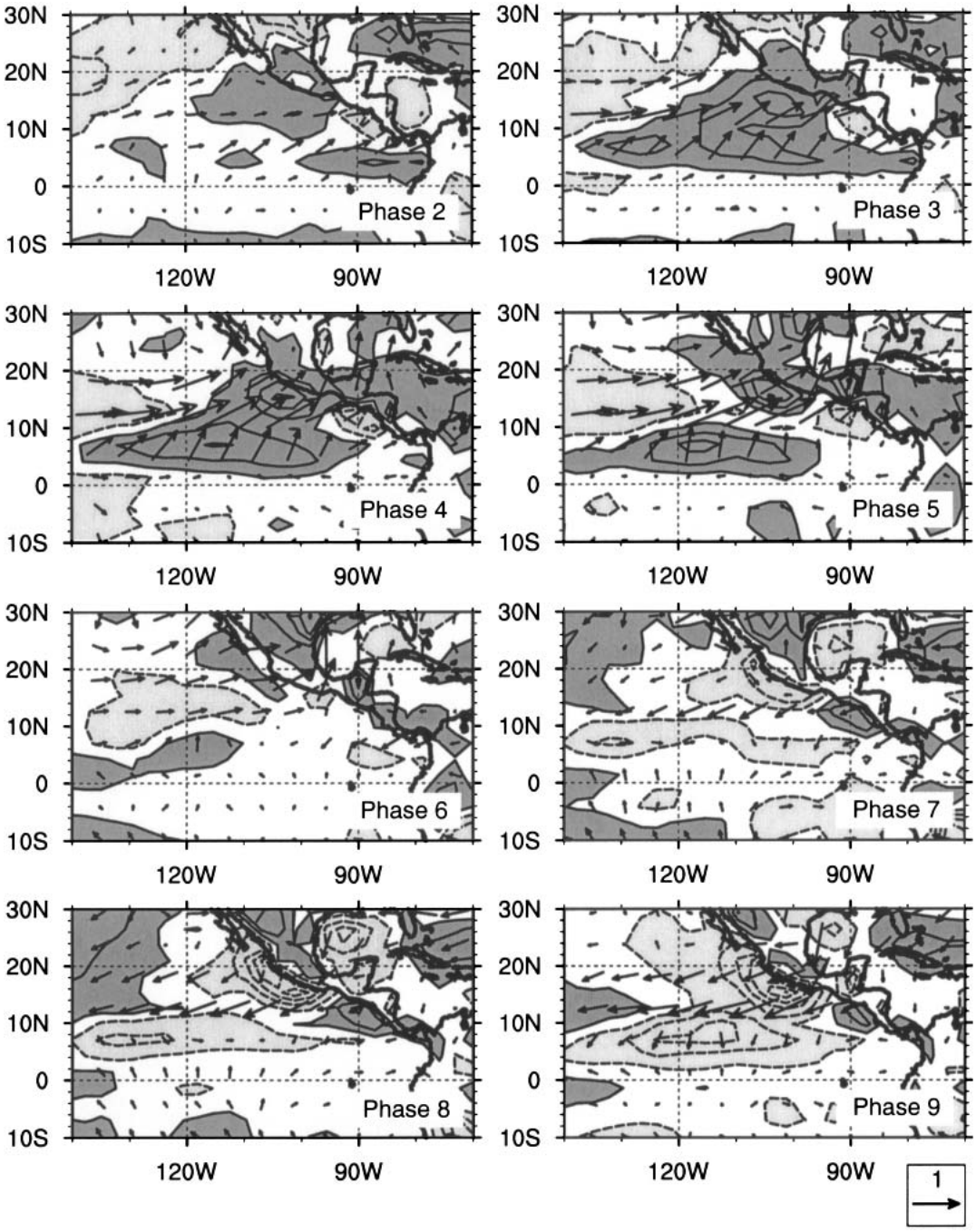

FIG. 10. Control simulation composite Jun–Oct ISO surface wind and latent heat flux anomalies as a function of phase. Flux contours are plotted every 4.0 W m^{-2}, starting at 2.0 W m^{-2}. Values greater (less) than 2.0 W m^{-2} (-2.0 W m^{-2}) are dark (light) shaded. The reference wind vector (m s^{-1}) is located at the bottom right.

tent heat fluxes during ISO events (not shown), as implied by Maloney and Sobel (2004). ISO-related westerly anomalies and enhanced latent heat fluxes in the waveguide of the west Pacific are associated with positive anomalies of surface pressure and divergence, which may provide dynamical suppression of precipitation there.

Latent heat flux and precipitation are correlated near 0.75 at zero lag in both observations and the control simulation in the east Pacific (Fig. 11), a statistically significant correlation at the 95% confidence level in both cases. The spread of latent heat flux anomalies at positive values is greater than that at negative values in both observations and in the control, and several very

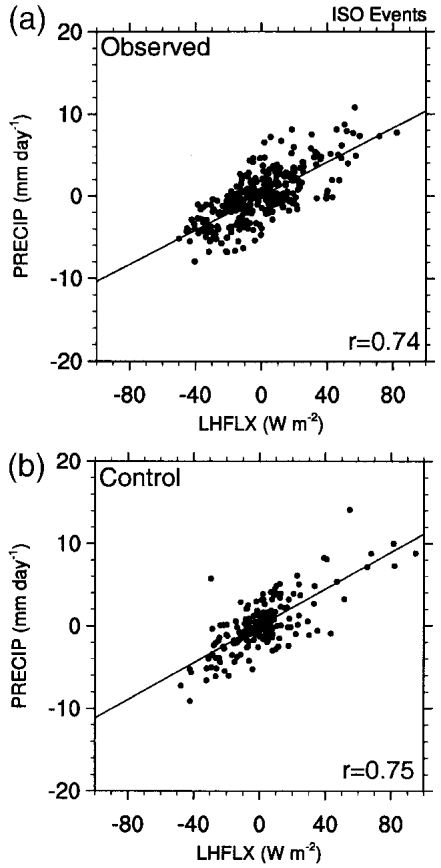

FIG. 11. Scatterplot of east Pacific warm pool precipitation vs latent heat flux anomalies during (a) observed and (b) control simulation ISO events. Each dot represents one phase of a given event. The correlation coefficients are indicated on the plot. Regression coefficients for observations and the control simulation are 0.10 and 0.11 (mm day^{-1} W^{-1} m^2), respectively.

strong positive latent heat flux anomaly events are present in both panels. The more bounded flux anomalies at negative values are somewhat imposed in the model due to the minimum wind speed requirement of 2 m s^{-1} in the model latent heat flux parameterization. When surface specific humidity deficit variations in the bulk formula are small, this minimum wind speed requirement effectively bounds the latent heat flux (e.g., Kiehl et al. 1998). The NCEP–NCAR reanalysis surface fluxes are also parameterized by a bulk formula, so the true spread of latent heat flux anomaly values may differ from the analysis product. The lack of strong negative values of the latent heat flux distribution is also physically reasonable since an unstable boundary layer with a net positive transfer of latent heat from the ocean to atmosphere is strongly preferred in this region. We plan to conduct a more thorough analysis of ISO-related latent heat flux variability over the tropical east Pacific in future work by using the Tropical Atmosphere–Ocean buoy array at 95°W and by using data from the EPIC2001 experiment.

Variations in control simulation surface latent heat flux over the east Pacific warm pool during ISO events are dominated by variations in surface wind speed. Figure 12 shows the relative magnitudes of the composite terms $\overline{\Delta q}|V|'$ and $\Delta q'|\overline{V}|$that are related to those obtained by linearization of the surface latent heat flux bulk formula,

$$\mathrm{LH}' = \rho L C_H(\overline{\Delta q}|V|' + \Delta q'|\overline{V}|), \qquad (1)$$

where ρ is the density of near-surface air, C_H is the exchange coefficient, L is the latent heat of vaporization, Δq represents the difference between the surface saturation specific humidity and the lowest model level specific humidity, and $|V|$ represents the lowest model level wind speed. Overbars represent an average of unfiltered variables over all nine phases of a given ISO event. The terms were arbitrarily scaled by the same factor that approximates $\rho C_H L$. Variations in wind speed clearly dominate variations in latent heat flux, whereas specific humidity deficit variations produce negligible flux variations (Fig. 12). These results prove that intraseasonal latent heat flux variations in the control simulation are primarily wind induced, consistent with observed east Pacific ISO variability (ME03). As noted earlier, a strong degree of asymmetry exists between phases one and nine of the control simulation east Pacific ISO composite life cycle that is readily apparent in this composite of latent heat flux contributions.

The above results suggest that east Pacific intraseasonal precipitation variations in the control simulation are supported by a wind–evaporation feedback mechanism broadly related to that proposed by Neelin et al. (1987) and Emanuel (1987). Whereas easterly anoma-

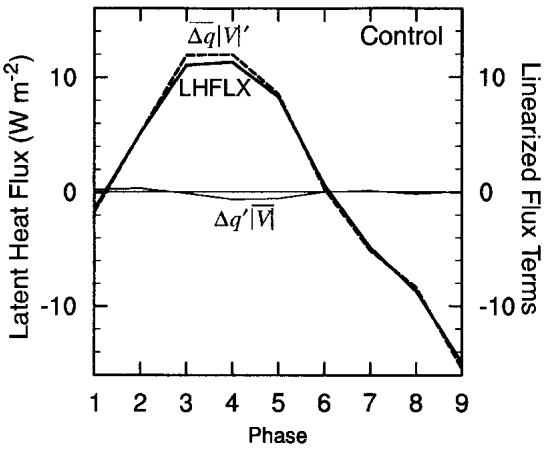

FIG. 12. Control simulation composite ISO latent heat flux anomalies and linearized latent heat flux terms for an approximate 5° × 5° averaging box centered at 14°N, 102°W. The flux terms are scaled consistently to provide an indication of their relative magnitudes. Primes represent intraseasonal anomalies and bars indicate an average over all nine phases of an ISO life cycle.

lies are associated with enhanced fluxes in the theories of Neelin et al. (1987) and Emanuel (1987), east Pacific westerly anomalies in the control simulation and observations are associated with enhanced latent heat fluxes that may support convection. The results here are more consistent with the ISO model developed by Raymond (2001), or with the boreal winter west Pacific modeling results of Maloney and Sobel (2004) that suggested a more generalized nonlinear wind–evaporation feedback mechanism. In both of these modeling frameworks, enhanced latent heat fluxes are associated with surface westerly anomalies, consistent with results derived in numerous observational studies (e.g., Lin and Johnson 1996; Jones and Weare 1996; Cronin and McPhaden 1997; Zhang and McPhaden 2000). Maloney and Sobel (2004) suggest a nonlinear wind–evaporation feedback mechanism in which horizontal advection transports moisture from regions of strong surface evaporation (surface westerly perturbations) into regions of enhanced ISO convection. The EPIC2001 results of Raymond et al. (2003) are also consistent with those found here, with a tendency for surface westerly anomalies to be associated with increased east Pacific warm pool latent heat fluxes and deep convection. Some of the convective variability observed during EPIC appears to have been modulated by the ISO (E. Maloney 2003, unpublished manuscript).

c. *ISO composites: Impact of wind–evaporation feedback*

We will now examine a composite ISO life cycle in the fixed-EVAP simulation to provide further evidence that wind–evaporation feedback is important for producing realistic summertime eastern North Pacific precipitation variability. Composite ISO precipitation and wind anomalies for the fixed-EVAP simulation are shown in Fig. 13, with the strongest anomalies occurring over land. Oceanic variations in precipitation are considerably weaker than those in the control simulation (Fig. 9). These results support the hypothesis that wind-induced heat flux variations forced by anomalies in the low-level flow are important for producing realistic intraseasonal precipitation variations over the east Pacific warm pool and may help explain the strong observed correlation there between intraseasonal latent heat flux and precipitation (ME03). Surprisingly, strong anomalies in the low-level flow still exist in the fixed-EVAP simulation. These anomalies appear to be related (to some extent) to precipitation anomalies over land. This probable coupling is most apparent during phase five, and a similar strong forcing of circulation anomalies by land precipitation may also be apparent during phase five of the control life cycle (Fig. 9). This close relationship between precipitation over land and flow anomalies over the ocean may help explain the relatively small differences in surface zonal wind variance between the control and fixed-EVAP simulations in Fig. 6.

An analysis of composite perturbation available potential energy (PAPE) generation further supports the contention that model large-scale circulation anomalies are primarily supported by diabatic heating anomalies (Q_1') over land. PAPE is generated where a positive covariance between perturbation temperature and diabatic heating occurs that reinforces the temperature perturbation and generates potential energy that is available to drive eddy motions. PAPE generation is calculated by

$$\frac{\partial P}{\partial t} = \frac{\lambda \overline{Q_1' T'}}{\overline{T}} . \tag{2}$$

Overbars indicate an average over all nine phases of an individual ISO event, and primes represent perturbations from this mean; λ is given by $\Gamma_d/(\Gamma_d - \Gamma)$ where Γ is the observed lapse rate, Γ_d is the dry-adiabatic lapse rate, and T is temperature. The PAPE analysis is described in more detail in ME03. Figure 14 shows composite PAPE generation for control and fixed-EVAP ISO events. PAPE generation is vertically averaged in this figure. Unlike observed ISO events where PAPE generation maximizes over the east Pacific warm pool (e.g., Fig. 6 of ME03), PAPE generation in the control and fixed-EVAP simulations maximizes over Mexico and Central America. Composite PAPE generation is somewhat weaker in the fixed-EVAP simulation than the control simulation. The association of circulation anomalies with atmospheric latent heating over land is confirmed by these results, however. Because interactive surface latent heat fluxes are retained over land in the fixed-EVAP simulation, relatively high flux anomalies greater than 6 W m^{-2} occur there during certain ISO phases (e.g., phase five, not shown). These enhanced fluxes may help to support precipitation anomalies over land in the model. However, neither these surface flux variations nor the characteristics of the land surface itself appear at first order to control intraseasonal precipitation variations over land, and consequently the forcing of the large-scale circulation.

d. *Impact of surface type and orography*

Figure 15 shows intraseasonal surface zonal wind variance from the no-land simulation. Recall that land points within the domain 10°–30°N, 80°–120°W are set to ocean in this simulation and latent heat fluxes and surface temperature are prescribed. Surface geopotential heights are also prescribed to be the same as the control. Intraseasonal zonal wind variance in the no-land simulation increases slightly compared to that in the control (Fig. 15), although warm pool precipitation variance remains significantly higher in the control than in the no-land simulation (not shown). These results indicate that the representation of model orography rather than land surface type is likely responsible for the intraseasonal variations of precipitation over Cen-

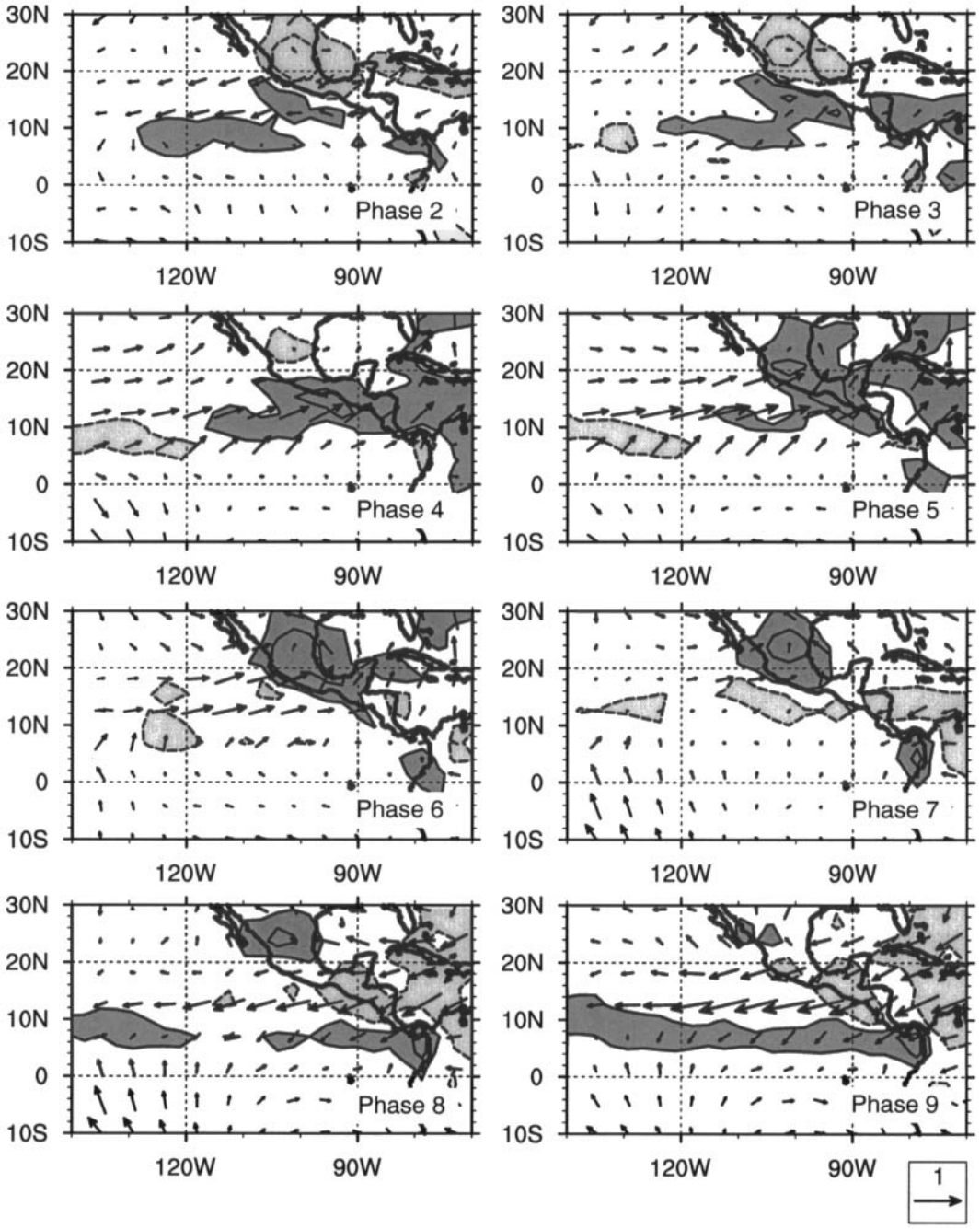

FIG. 13. As in Fig. 9 except for the fixed-EVAP simulation.

tral America that lead to strong PAPE generation there.

Figure 16 shows that intraseasonal precipitation variance in the no-land simulation is concentrated at the foot of the model representation of the Sierra Madre. Strong localized variance maxima in relative vorticity and surface divergence are collocated with these precipitation maxima (not shown). A composite ISO event in the no-land simulation shows strong localized relative vorticity anomalies at the foot of the Sierra Madre associated with ISO-related variations in the large-scale flow impinging on Central America (not shown). Positive (negative) vorticity anomalies are associated with anomalous surface convergence (divergence), consistent with the influence of surface drag on the low-level flow (not shown). Mozer and Zehnder (1996, hereafter MZ96) argue that the low-level flow impinging on the Sierra Madre is effectively blocked within the relatively

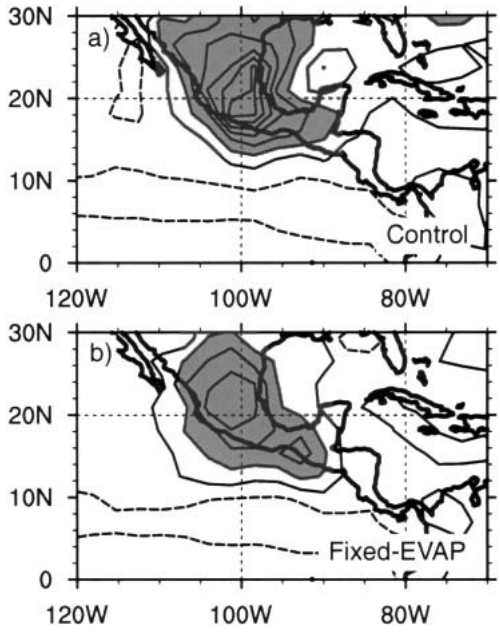

FIG. 14. ISO composite vertically averaged production of PAPE from the (a) control and (b) fixed-EVAP simulations. The contour interval is 4.0 $m^2\ s^{-2}\ day^{-1}$, starting at 2.0 $m^2\ s^{-2}\ day^{-1}$. Values greater (less) than 6.0 $m^2\ s^{-2}\ day^{-1}$ ($-6.0\ m^2\ s^{-2}\ day^{-1}$) are shaded.

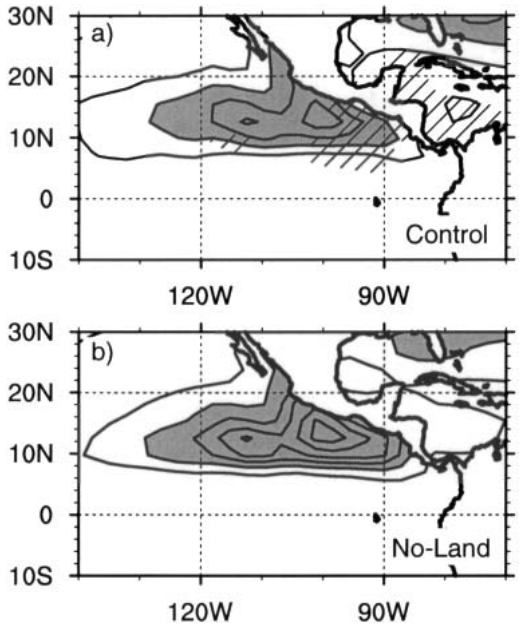

FIG. 15. Jun–Oct 30–90-day surface zonal wind variance (a) the control simulation and (b) the no-land simulation. The contour interval is 0.8 $m^2\ s^{-2}$. Values greater than 1.6 $m^2\ s^{-2}$ are shaded. Diagonal lines in (a) indicate where the control variance falls below the lower 95% confidence limit on the no-land variance. All grid cells in the no-land simulation within the domain 10°–30°N, 80°–120°W are set to ocean, although the original surface geopotential heights are retained. Land outlines within this region in (b) are only shown for reference.

high Rossby number and low Froude number regime characteristic of southern Mexico and Central America (e.g., Pierrehumbert and Wyman 1985). MZ96 further show, using a model with an idealized representation of the Sierra Madre, that flow is forced around the southern edge of the mountain range. Potential vorticity constraints demand a concentrated and substantially sheared flow at the southern edge of the range. Although the resolution of orography in our model is coarser than that used in MZ96, the characteristics of the flow in the GCM show some similarity to that in MZ96. The interactions between the large-scale flow and orography in the CAM2.0.1 would likely be altered if the mountains of Central America were better resolved. Another interesting experiment for future work would be to remove Central American orography to determine to what extent oceanic precipitation and latent heat flux anomalies in the model would exist in the absence of orographic influence.

Maloney (2002) showed that the RAS convection scheme used here responds strongly to perturbations in surface convergence. Strong convergence perturbations accompany the vorticity anomalies at the southern end of the Sierra Madre, which may help to force strong precipitation variations there in the model. We have verified that the GCM convection parameterization rather than the large-scale precipitation scheme is primarily responsible for the precipitation anomalies over Central America.

e. Sensitivity to analysis technique

As a check to ensure that our compositing technique is not responsible for the differences between the control and fixed-EVAP simulations that we find, we have also analyzed east Pacific intraseasonal precipitation and wind variations using an alternate method. Control and fixed-EVAP simulation intraseasonal surface winds and precipitation were regressed onto the leading EOF of east Pacific intraseasonal precipitation at zero

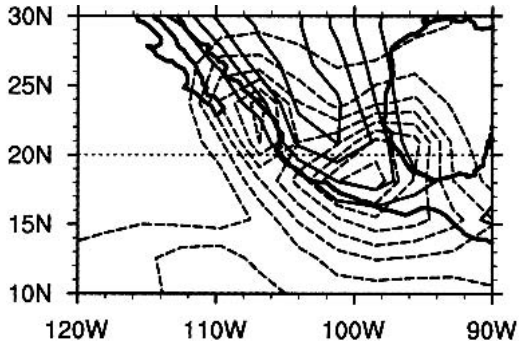

FIG. 16. Jun–Oct 30–90-day precipitation variance from the no-land simulation. The contour interval is 2 $mm^2\ day^{-2}$. Surface height contours are also shown, and are consistent with Fig. 1. Land outlines are only shown for reference.

lag. Results (not shown) are quite consistent with those in the composite life cycles shown above, with the control simulation fields very much resembling phase four of the composite life cycle shown in Fig. 9 and the fixed-EVAP fields resembling phase four or five of the corresponding composite life cycle (Fig. 13). Maximum regressed intraseasonal precipitation anomalies in the control simulation are about twice as strong as those for the fixed-EVAP simulation, although this disparity is much greater directly over the east Pacific warm pool. Differences in the strength of low-level wind anomalies were stronger than for precipitation, also consistent with the results shown above. Our results are therefore not sensitive to the analysis technique used. We note, however, that our global index explains only a portion of the local variance over the east Pacific, and a local EOF analysis is more likely to be influenced by subseasonal processes that are inherently regional in nature and unrelated to global modes of variability.

f. The role of convergence

Although our model results suggest the importance of wind-induced latent heat flux variations in forcing intraseasonal convection over the east Pacific warm pool during summertime, we have not ruled out that other factors are important as well. For example, ME03 showed a strong correlation between NCEP–NCAR reanalysis surface convergence and negative outgoing longwave radiation (OLR) anomalies during east Pacific ISO events. Similar scatterplots as shown in Fig. 11, but now for precipitation versus surface convergence, are shown in Fig. 17. Observed precipitation and convergence anomalies are now collocated to be consistent with the strong collocated correlations of divergence and OLR as described by ME03. The observed averaging box is centered at 11°N, 99°W and the model boxes are centered at 14°N, 102°W. Observed intraseasonal precipitation and convergence are correlated at 0.65—a correlation significant at the 95% confidence limit. Surface convergence and precipitation are also significantly correlated in the control (0.81) and fixed-EVAP (0.76) simulations, suggesting we cannot rule out that surface convergence helps to support east Pacific deep convection during an ISO life cycle.

Some differences in the relationship between intraseasonal surface convergence and precipitation do exist between the two simulations, however. Notice that the regression coefficient (slope) in the control simulation is comparable to that observed. The regression coefficient in the fixed-EVAP simulation is reduced by about a third from the control. These results suggest that, even if surface convergence were an important mechanism for supporting east Pacific intraseasonal convection variations, support from surface latent heat exchange is necessary to produce the observed relationship between surface convergence and intraseasonal convection.

Maloney and Kiehl (2002b) described modeling results in which inclusion of an interactive slab ocean led to an amplification of summertime east Pacific intraseasonal variability relative to a control simulation with prescribed climatological SSTs. Although we have not conducted such coupled simulations here, Maloney and

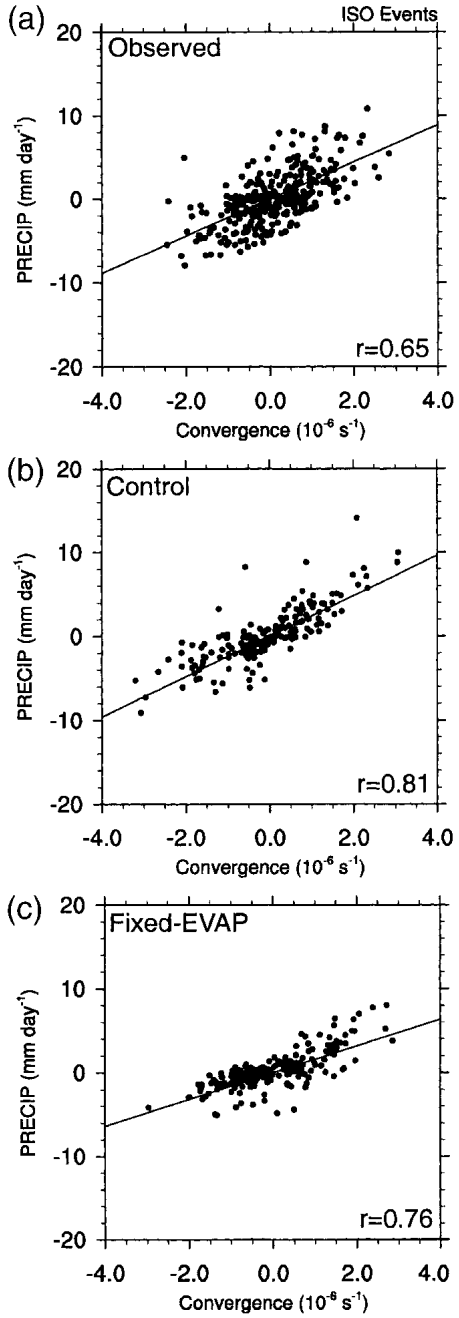

FIG. 17. Scatterplot of east Pacific warm pool precipitation vs surface convergence anomalies during (a) observed, (b) control simulation, and (c) fixed-EVAP simulation ISO events. Each dot represents one phase of a given event. The correlation coefficients are indicated on the plot. Regression coefficients for observations, the control simulation, and the fixed-EVAP simulation are 2.22, 2.40, and 1.59 (mm day^{-1} s^{1} 10^{6}), respectively.

Sobel (2004) conducted sensitivity experiments that coupled the NCAR CAM2.0.1 with RAS convection (our model) to slab oceans of varying depth. A brief examination of these runs shows a modest amplification of east Pacific summertime intraseasonal precipitation variability when coupling to a slab ocean, with the strongest amplification of about 50% occurring for a slab ocean depth of 10 m (not shown). No shift in the location of highest variance occurs between the control and slab ocean simulations. These results are consistent with those of Maloney and Kiehl (2002b) that demonstrate an amplification of intraseasonal precipitation variability over the east Pacific when coupling to an interactive ocean. Precipitation variability in the coupled CAM2.0.1 run is stronger than observed, however. One reason for this discrepancy may be that our CAM2.0.1 climatological SST control simulation produces more realistic east Pacific intraseasonal variability than did the comparable simulation described in Maloney and Kiehl [the NCAR Community Climate Model 3.6 (CCM3.6) with RAS convection]. The NCAR CCM3.6 with RAS convection was only able to produce realistic intraseasonal variability when coupled to an interactive ocean. These differences suggest some degree of model dependence to the results we describe here.

5. Conclusions

Wind-induced variations in surface latent heat flux are important for producing realistic June–October intraseasonal precipitation variability over the northeast Pacific warm pool in the National Center for Atmospheric Research Community Atmosphere Model 2.0.1 with relaxed Arakawa–Schubert convection. A control simulation with prescribed climatological SSTs and interactive surface fluxes produces intraseasonal eastern North Pacific wind and precipitation variations that are of similar magnitude and structure to those associated with the observed intraseasonal oscillation (ISO). Periods of low-level westerly wind anomalies in the model are associated with enhanced surface latent heat fluxes and enhanced precipitation, as in observations. Variations in surface wind speed dominate the surface flux anomalies. A simulation in which eastern North Pacific oceanic latent heat fluxes are prescribed by their climatological values produces intraseasonal precipitation variations significantly lower than those in the control simulation and in observations. These results support the observational findings of ME03, who suggested that wind-induced latent heat flux variability is a significant driver of ISO-related convective variability over the northeast Pacific warm pool during Northern Hemisphere summer. These results also support the findings of Raymond et al. (2003), who showed a strong correlation between latent heat flux and precipitation anomalies over the eastern north Pacific warm pool during the EPIC2001 experiment.

Summertime eastern North Pacific intraseasonal wind variability does not vary significantly between the control and fixed-evaporation simulations. The simulated wind variability appears to be the result of strong coupling between the east Pacific flow and precipitation over Central America in the model. Observations suggest however that such a strong coupling does not exist. The coarse resolution of Central American orography in the model may contribute to the unrealistic coupling, although deficiencies in how the model convection parameterization responds to orographically forced flows may also heighten model precipitation variability over land. A simulation without significant land surface feedbacks over Central America, but with realistic surface geopotential heights, verifies that orography is the most likely forcing agent for inland model intraseasonal heating anomalies rather than interactions with land surface heat fluxes.

The results presented here do not rule out surface convergence as an important forcing mechanism for summertime eastern North Pacific convection. Such a link was suggested by ME03. However, the relationship between convergence and precipitation appears to weaken when model latent heat fluxes are set to climatology. Although surface convergence may be important for forcing precipitation variations in the model, realistic model intraseasonal variability is not produced without the aid of anomalous surface latent heat fluxes.

Future work will examine the role of surface convergence in supporting intraseasonal convection variations over the eastern North Pacific warm pool. Idealized experiments could be designed to alter surface drag in the model to gauge its influence on intraseasonal variability. These experiments will need to be designed carefully to limit changes to the model climate over the eastern north Pacific and elsewhere, however. Future work will also examine the importance of cloud–radiative feedbacks for producing realistic intraseasonal variability over the east Pacific warm pool. Sobel and Gildor (2003) used an idealized model to suggest that longwave cloud feedbacks may be important for sustaining intraseasonal precipitation oscillations in the Tropics [Lin and Mapes (2004) have more recently found that shortwave cloud feedbacks dominate longwave feedbacks during ISO events, however]. The combination of longwave and shortwave cloud feedbacks, and surface latent heat flux variations, result in a redistribution of energy between the ocean and atmosphere during ISO events that may strongly feedback onto and/or force intraseasonal convection variations.

Acknowledgments. We thank two anonymous reviewers for their helpful comments on this manuscript. CMAP precipitation and NCEP/NCAR reanalysis data were provided by the NOAA–CIRES Climate Diagnostics Center, Boulder, Colorado. The authors wish to thank the TRMM Science Data and Information System and the Distributed Active Archive Center for pro-

viding the TRMM precipitation fields. Supercomputing resources were provided by the National Center for Atmospheric Research, Boulder, Colorado. This work was supported by the Climate Dynamics Program of the National Science Foundation under Grants ATM-0327460 (EDM) and ATM-0002322 (SKE). Any opinions, findings, conclusions, or recommendations expressed in this paper are those of the authors and do not necessarily reflect the views of the sponsors.

REFERENCES

Betts, A. K., 1976: The thermodynamic transformation of the tropical sub-cloud layer by precipitation and downdrafts. *J. Atmos. Sci.,* **33,** 1008–1020.

Bond, N. A., and G. A. Vecchi, 2003: The influence of the Madden–Julian oscillation on precipitation in Oregon and Washington. *Wea. Forecasting,* **18,** 600–613.

Cronin, M. F., and M. J. McPhaden, 1997: The upper ocean heat balance in the western equatorial Pacific warm pool during September–December 1992. *J. Geophys. Res.,* **102,** 27 567–27 587.

Emanuel, K. A., 1987: An air–sea interaction model of intraseasonal oscillations in the tropics. *J. Atmos. Sci.,* **44,** 2324–2340.

Hack, J. J., 1994: Parameterization of moist convection in the National Center for Atmospheric Research community climate model (CCM2). *J. Geophys. Res.,* **99,** 5551–5568.

Hendon, H. H., and M. L. Salby, 1994: The life cycle of the Madden–Julian oscillation. *J. Atmos. Sci.,* **51,** 2225–2237.

Higgins, R. W., and W. Shi, 2001: Intercomparison of the principal modes of interannual and intraseasonal variability of the North American monsoon system. *J. Climate,* **14,** 403–417.

Jones, C., and B. C. Weare, 1996: The role of low-level moisture convergence and ocean latent heat fluxes in the Madden and Julian oscillation: An observational analysis using ISCCP data and ECMWF analyses. *J. Climate,* **9,** 3086–3104.

Kalnay, E., and Coauthors, 1996: The NCEP/NCAR 40-Year Reanalysis Project. *Bull. Amer. Meteor. Soc.,* **77,** 437–471.

Kayano, M. T., and V. E. Kousky, 1999: Intraseasonal (30–60 day) variability in the global Tropics: Principal modes and their evolution. *Tellus,* **51A,** 373–386.

Kiehl, J. T., J. J. Hack, G. B. Bonan, B. A. Boville, D. L. Williamson, and P. J. Rasch, 1998: The National Center for Atmospheric Research Community Climate Model: CCM3. *J. Climate,* **11,** 1131–1149.

Knutson, T. R., and K. M. Weickmann, 1987: 30–60 day atmospheric circulations: Composite life cycles of convection and circulation anomalies. *Mon. Wea. Rev.,* **115,** 1407–1436.

Kummerow, C., and Coauthors, 2000: The status of the Tropical Rainfall Measuring Mission (TRMM) after two years in orbit. *J. Appl. Meteor.,* **39,** 1965–1982.

Kutzbach, J. E., 1967: Empirical eigenvectors of sea-level pressure, surface temperature, and precipitation complexes over North America. *J. Appl. Meteor.,* **6,** 791–802.

Lin, J.-L., and B. E. Mapes, 2004: Radiation budget of the tropical intraseasonal oscillations. *J. Atmos. Sci.,* **61,** 2050–2062.

Lin, X., and R. H. Johnson, 1996: Kinematic and thermodynamic characteristics of the flow over the western Pacific warm pool during TOGA COARE. *J. Atmos. Sci.,* **53,** 695–715.

Madden, R. A., and P. R. Julian, 1994: Observations of the 40–50 day tropical oscillation—A review. *Mon. Wea. Rev.,* **122,** 814–837.

Magaña, V., J. A. Amador, and S. Medina, 1999: The midsummer drought over Mexico and Central America. *J. Climate,* **12,** 1577–1588.

Maloney, E. D., 2002: An intraseasonal oscillation composite life cycle in the NCAR CCM3.6 with modified convection. *J. Climate,* **15,** 964–982.

——, and D. L. Hartmann, 1998: Frictional moisture convergence in a composite life cycle of the Madden–Julian oscillation. *J. Climate,* **11,** 2387–2403.

——, and ——, 2000: Modulation of eastern north Pacific hurricanes by the Madden–Julian oscillation. *J. Climate,* **13,** 1451–1460.

——, and ——, 2001: The sensitivity of intraseasonal variability in the NCAR CCM3 to changes in convective parameterization. *J. Climate,* **14,** 2015–2034.

——, and J. T. Kiehl, 2002a: MJO-related SST variations over the tropical eastern Pacific during Northern Hemisphere summer. *J. Climate,* **15,** 675–689.

——, and ——, 2002b: Intraseasonal eastern Pacific precipitation and SST variations in a GCM coupled to a slab ocean model. *J. Climate,* **15,** 2989–3007.

——, and S. K. Esbensen, 2003: The amplification of east Pacific Madden–Julian oscillation convection and wind anomalies during June–November. *J. Climate,* **16,** 3482–3497.

——, and A. H. Sobel, 2004: Surface fluxes and ocean coupling in the tropical intraseasonal oscillation. *J. Climate,* **17,** 4368–4386.

Mapes, B. E., T. T. Warner, M. Xu, and A. J. Negri, 2003: Diurnal patterns of rainfall in northwestern South America. Part I: Observations and context. *Mon. Wea. Rev.,* **131,** 799–812.

Milliff, R. F., W. G. Large, J. Morzel, G. Danabasoglu, and T. M. Chen, 1999: Ocean general circulation model sensitivity to forcing from scatterometer winds. *J. Geophys. Res.,* **104,** 11 337–11 358.

Moorthi, S., and M. J. Suarez, 1992: Relaxed Arakawa–Schubert. A parameterization of moist convection for general circulation models. *Mon. Wea. Rev.,* **120,** 978–1002.

Mozer, J. B., and J. A. Zehnder, 1996: Lee vorticity production by large-scale tropical mountain ranges. Part I: Eastern north Pacific tropical cyclogenesis. *J. Atmos. Sci.,* **53,** 521–538.

Neelin, J. D., I. M. Held, and K. H. Cook, 1987: Evaporation–wind feedback and low-frequency variability in the tropical atmosphere. *J. Atmos. Sci.,* **44,** 2341–2348.

Pierrehumbert, R. T., and B. Wyman, 1985: Upstream effects of mesoscale mountains. *J. Atmos. Sci.,* **42,** 977–1003.

Raymond, D. J., 2001: A new model of the Madden–Julian oscillation. *J. Atmos. Sci.,* **58,** 2807–2819.

——, G. B. Raga, C. S. Bretherton, J. Molinari, C. Lopez-Carillo, and Z. Fuchs, 2003: Convective forcing in the intertropical convergence zone of the eastern Pacific. *J. Atmos. Sci.,* **60,** 2064–2082.

Sobel, A. H., and H. Gildor, 2003: A simple time-dependent model of SST hotspots. *J. Climate,* **16,** 3978–3992.

Sud, Y. C., and A. Molod, 1988: The roles of dry convection, cloud-radiation feedback processes, and the influence of recent improvements in the parameterization of convection in the GLA GCM. *Mon. Wea. Rev.,* **116,** 2366–2387.

Xie, P., and P. A. Arkin, 1996: Analyses of global monthly precipitation using gauge observations, satellite estimates, and numerical model predictions. *J. Climate,* **9,** 840–858.

Zhang, C., and M. J. McPhaden, 2000: Intraseasonal surface cooling in the equatorial western Pacific. *J. Climate,* **13,** 2261–2276.

Zhang, G. J., and N. A. McFarlane, 1995: Sensitivity of climate simulations to the parameterization of cumulus convection in the Canadian Climate Centre General Circulation Model. *Atmos.-Ocean,* **33,** 407–446.